

Supplementary information

Protein dynamics from accurate low-field site-specific longitudinal and transverse relaxation

*Pavel Kaderávek,¹ Nicolas-Bolik Coulon,¹ Samuel F. Cousin,¹ Thorsten Marquardsen,²
Jean-Max Tyburn,³ Jean-Nicolas Dumez,⁴ Fabien Ferrage^{1,*}*

- 1) Laboratoire des Biomolécules, LBM, Département de chimie; École normale supérieure, PSL University, Sorbonne Université, CNRS; 75005 Paris, France.*
- 2) Bruker BioSpin GmbH, Silberstreifen 4, 76287 Rheinstetten, Germany.*
- 3) Bruker BioSpin, 34 rue de l'Industrie BP 10002, 67166 Wissembourg Cedex, France.*
- 4) CEISAM, CNRS, Université de Nantes, 44300 Nantes, France*

Fabien.Ferrage@ens.fr

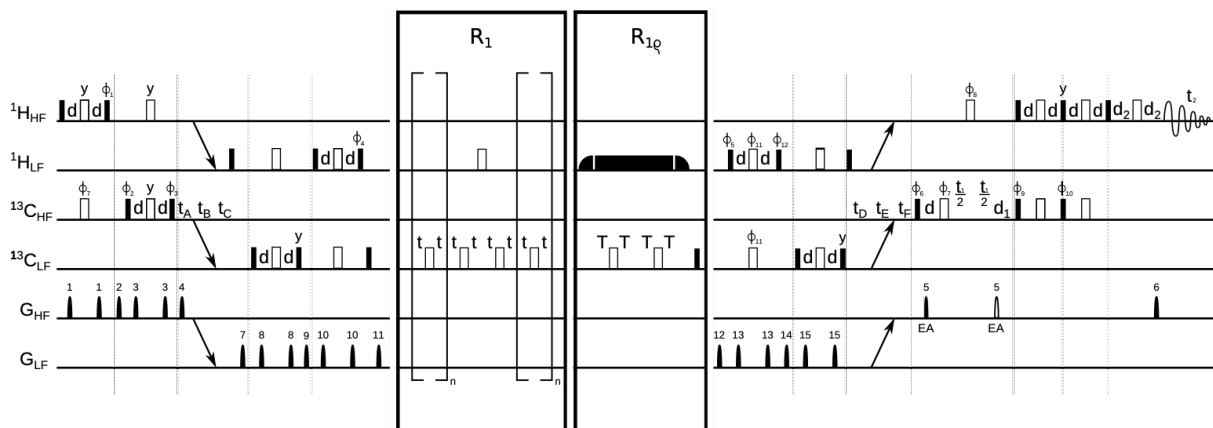


Figure S1. NMR pulse sequences used to measure the proton longitudinal and transverse relaxation rates at 0.33 T using a two-field NMR spectrometer. The pulse programs for R_1 and R_{1Q} differs only by the block in the central part of the pulse program. The HF and LF subscripts refer to rf-pulses and gradients applied at high-field and low field. The narrow filled and wide-open pulses represent $\pi/2$ and π pulses, respectively. The rf-pulses are applied along the x axis of the rotating frame, unless specified otherwise. The delay d is equal to $1/(4J)$, where $J=135$ Hz is the scalar-coupling constant for methyl ^{13}C -H spin pair. t_1 is the incremented delay for chemical shift labeling in the indirect dimension, t_2 denotes the acquisition time during the direct signal detection. d_2 is a minimal delay to allow application of a gradient and gradient recovery delay. $t_c = 30\text{ms}$ and $t_h = 350$ ms are stabilization delays at the low and high field sample position. The sample transfer between high-field and low-field positions are approximately 120 ms long (delays t_h and t_c) and they are preceded with a waiting delays (t_a and t_b) required by the pneumatic shuttling system (approximately 40 ms). The delay t during the longitudinal relaxation experiment was 5 ms long and various relaxation delays (20, 40, 60, 80, and 120 ms) were achieved by applying different numbers n of repeats of the block in the square brackets. The wide filled box represents a spin lock irradiation (total duration 4T). The durations of the spin lock used in our experiment for measurement of proton R_{1Q} relaxation rates were 0*, 15, 30, 50, 80, 115*, and 275 ms (where the star indicates relaxation delays repeated twice) applied with an amplitude of 5 kHz. They are flanked with 5 ms long adiabatic half passage ramps depicted by a filled quarter-elliptic shape. The gradients were applied for 0.8 ms with sine shape and following intensities at high field probe: $G_1 = 3.5$, $G_2 = 8.5$, $G_3 = 5.5$, $G_4 = 4.5$, $G_5 = \pm 10$, $G_6 = 5.025$ G/cm, and low field probe: $G_7 = 3.5$, $G_8 = 5.5$, $G_9 = 16.5$, $G_{10} = -7.5$, $G_{11} = 10.5$, $G_{12} = 3.25$, $G_{13} = -3.85$, $G_{14} = 6$, $G_{15} = 9.5$ G/cm. The pair of gradients G_5 were applied with opposite sign and their sign was alternated between individual t_1 increments accompanied with inversion of phases Φ_6 , Φ_7 , Φ_{10} and receiver phase in order to achieve quadrature detection in the indirect dimension in Echo-Antiecho manner. The phase cycles follow: $\Phi_1 = \{4\{y\}, 4\{-y\}\}$, $\Phi_2 = \{x, -x\}$, $\Phi_3 = \{8\{y\}, 8\{-y\}\}$, $\Phi_4 = \{32\{y\}, 32\{-y\}\}$, $\Phi_5 = x$ for R_1 , $\Phi_5 = \{64\{y\}, 64\{-y\}\}$ for R_{1Q} , $\Phi_6 = \{16\{y\}, 16\{-y\}\}$, $\Phi_7 = x$, $\Phi_8 = \{2\{x\}, 2\{-x\}\}$, $\Phi_9 = \{2\{x\}, 2\{-x\}\}$, $\Phi_{10} = \{2\{-y\}, 2\{y\}\}$, $\Phi_{11} = x$ for R_1 , $\Phi_{11} = x$ for R_{1Q} , $\Phi_{12} = y$ for R_1 , $\Phi_{12} = y$ for R_{1Q} , and receiver phase $\Phi_{rec} = \{X, -X, -X, X, -X, X, X, -X, -X, X, X, -X, -X, X, X, -X, X, -X, -X, X\}$ for R_1 , $\Phi_{rec} = \{X, -X, -X, X, -X, X, X, -X, -X, X, X, -X, -X, X, X, -X, X, -X, -X, X\}$ for R_{1Q} , where $X = \{x, -x, -x, x, -x, x, x, -x\}$.

Supplementary Information for Figure 1: NMR pulse program used to measure the carbon-13 R_1 and R_{10} relaxation rates

The sample movement between the high field (14.1 T) and the low field (0.33 T) centers can be divided into three events: waiting time required by the pneumatic shuttling system, duration of the sample movement, and stabilization delay after the sample reached the targeted other position. The delays were the same as presented in Figure S1 for the measurement of proton relaxation rates (times t_A , t_B , t_C , t_D , t_E , and t_F).

The gradient intensities used in the measurement of carbon-13 relaxation rates were at the high field probe: $G_1 = 3.5$, $G_2 = 8.5$, $G_3 = 5.5$, $G_4 = 4.5$, $G_5 = \pm 10$, $G_6 = 5.025$ G/cm, and low field probe: $G_7 = 5.5$, $G_8 = 3.5$, $G_9 = 9.5$, $G_{10} = -7.5$, $G_{11} = 16.5$, $G_{12} = -4.5$ G/cm. The pair of gradients G_5 were applied with opposite sign and their sign was alternated between individual t_i increments accompanied with inversion of phases Φ_6 , Φ_7 , Φ_{10} and receiver phase in order to achieve quadrature detection in the indirect dimension in Echo-Antiecho manner. The phase cycles follow: $\Phi_1 = \{4\{y\}, 4\{-y\}\}$, $\Phi_2 = \{x, -x\}$, $\Phi_3 = \{8\{y\}, 8\{-y\}\}$, $\Phi_4 = \{32\{y\}, 32\{-y\}\}$, $\Phi_5 = y$ for R_1 , $\Phi_5 = \{64\{y\}, 64\{-y\}\}$ for R_{10} , $\Phi_6 = \{16\{y\}, 16\{-y\}\}$, $\Phi_7 = x$, $\Phi_8 = \{2\{x\}, 2\{-x\}\}$, $\Phi_9 = \{2\{x\}, 2\{-x\}\}$, $\Phi_{10} = \{2\{-y\}, 2\{y\}\}$, $\Phi_{11} = x$ for R_1 , $\Phi_{11} = x$ for R_{10} , $\Phi_{12} = y$ for R_1 , $\Phi_{12} = y$ for R_{10} , and receiver phase $\Phi_{rec} = \{X, -X, -X, X, -X, X, X, -X\}$ for R_1 , $\Phi_{rec} = \{X, -X, -X, X, -X, X, X, -X, -X, X, X, -X, X, -X, -X, X\}$ for R_{10} , where $X = \{x, -x, -x, x, -x, x, x, -x\}$.

Table S1. Carbon-13 longitudinal and transverse relaxation rates. The residue number, longitudinal relaxation rate, transverse relaxation rate, predicted longitudinal and transverse relaxation rates simulated using dynamic parameters published earlier [1] are shown in the first, second, third, fourth, and fifth column, respectively.

residue	$R_1 (^{13}\text{C}) / \text{s}^{-1}$	$R_2 (^{13}\text{C}) / \text{s}^{-1}$	simulated $R_1 (^{13}\text{C}) / \text{s}^{-1}$	simulated $R_2 (^{13}\text{C}) / \text{s}^{-1}$
3	7.30 ± 0.48	7.29 ± 0.34	7.06	7.25
13	5.01 ± 0.23	5.12 ± 0.16	5.29	5.41
23	5.55 ± 0.23	5.72 ± 0.16	5.59	5.74
30	7.98 ± 0.57	7.34 ± 0.34	7.60	7.80
36	5.01 ± 0.23	5.23 ± 0.18	5.18	5.30
44	2.70 ± 0.10	2.76 ± 0.08	2.51	2.55
61	6.35 ± 0.28	6.42 ± 0.19	5.86	6.02

Table S2. Proton longitudinal and transverse relaxation rates. The residue number, longitudinal relaxation rate, transverse relaxation rate, predicted longitudinal and transverse relaxation rates simulated using dynamic parameters published earlier [1] are shown in the first, second, third, fourth, and fifth column, respectively.

residue	$R_1 (^1\text{H}) / \text{s}^{-1}$	$R_2 (^1\text{H}) / \text{s}^{-1}$	simulated $R_1 (^1\text{H}) / \text{s}^{-1}$	simulated $R_2 (^1\text{H}) / \text{s}^{-1}$
3	9.96 ± 0.56	11.88 ± 0.66	9.16	10.13
13	7.02 ± 0.29	7.76 ± 0.29	6.48	7.07
23	7.54 ± 0.28	9.24 ± 0.30	7.76	8.56
30	9.45 ± 0.56	10.88 ± 0.64	9.32	10.26
36	6.56 ± 0.27	7.30 ± 0.29	6.55	7.15
44	3.72 ± 0.16	3.99 ± 0.11	3.44	3.68
61	7.93 ± 0.32	8.66 ± 0.32	7.88	8.72

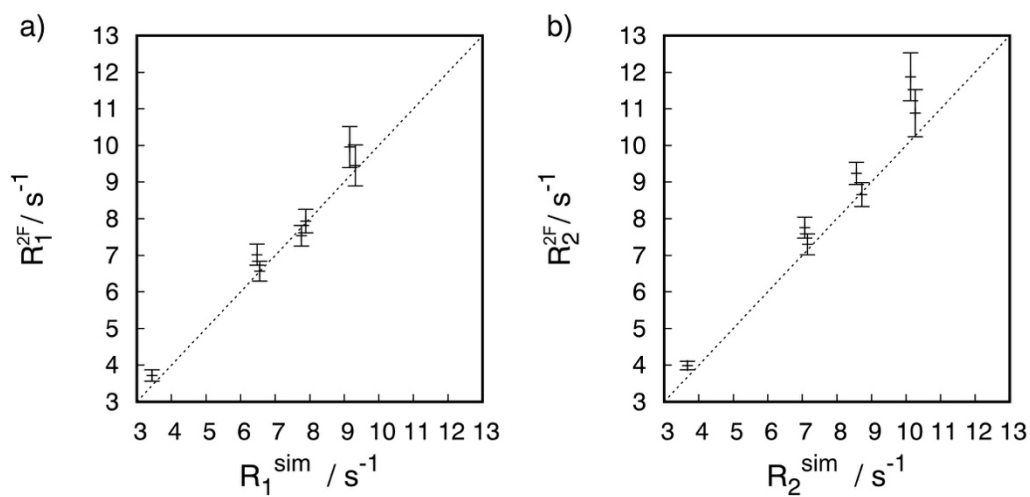


Figure S2. Correlation plot between the experimental (R_1 , R_2) and simulated (R_1^{sim} , R_2^{sim}) values of proton longitudinal (a) and transverse (b) relaxation rates. The simulations of the relaxation rates were performed using parameters published earlier [1]. The dashed lines represent the coincidence of experimental and simulated rates.

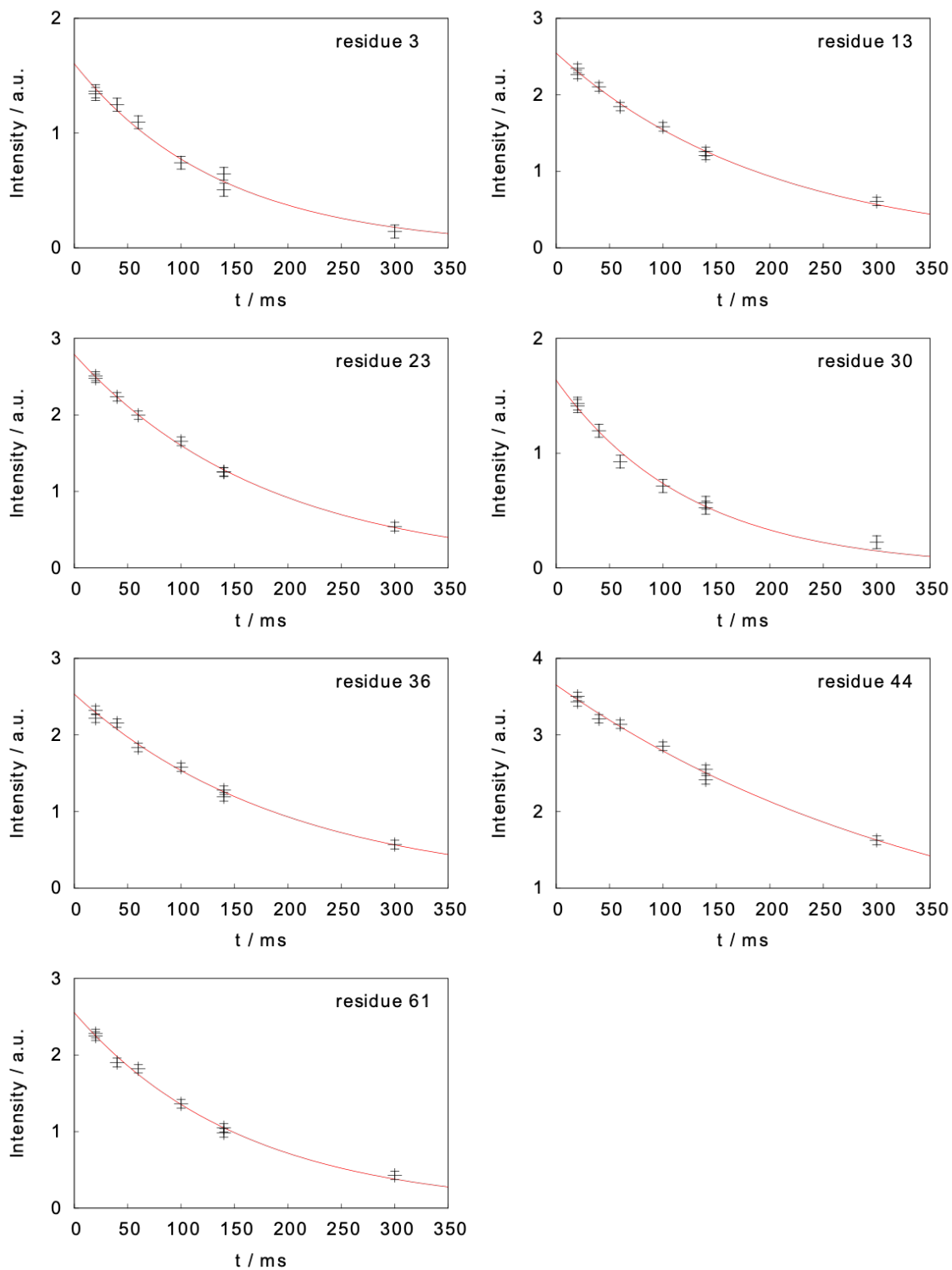


Figure S3. Measured intensity decays in the two-field NMR experiment for the measurement of carbon-13 longitudinal relaxation rates. Intensities are shown as black crosses together with their experimental uncertainty, the red curves represent the fitted mono-exponential decay.

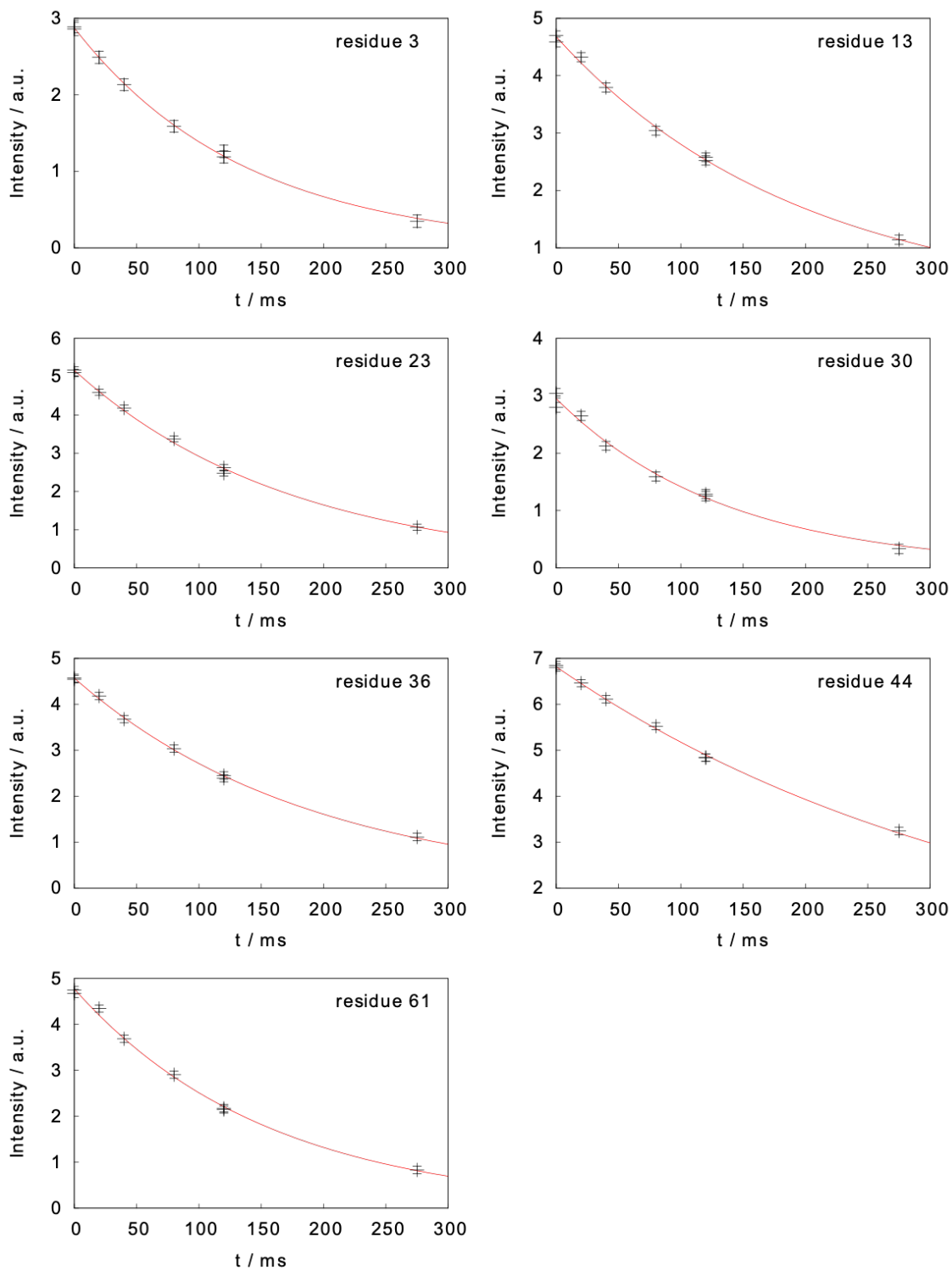


Figure S4. Measured intensity decays in the two-field NMR experiment for the measurement of carbon-13 R_{ρ} relaxation rates. Intensities are shown as black crosses together with their experimental uncertainty, the red curves represent the fitted mono-exponential decay.

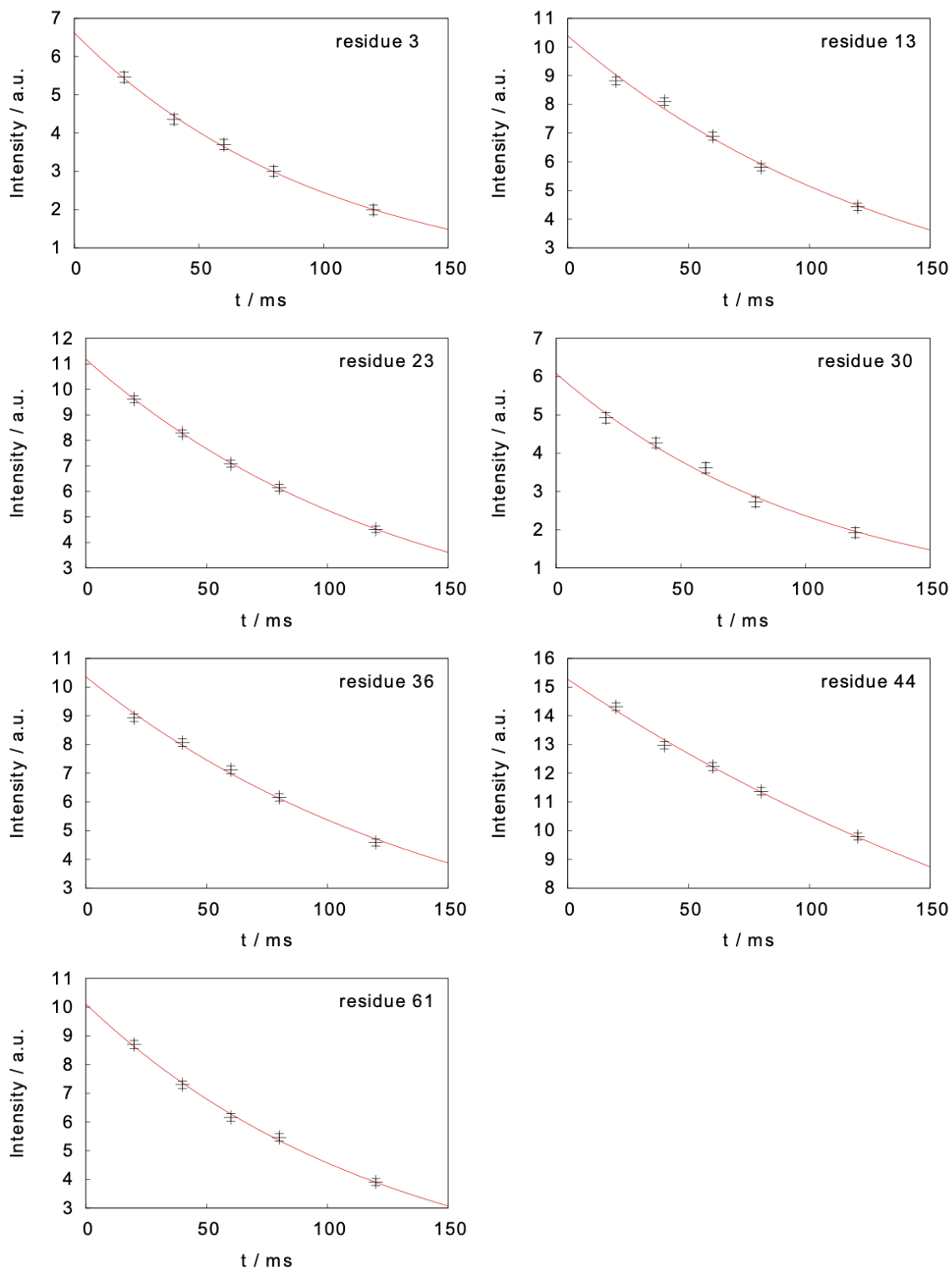


Figure S5. Measured intensity decays in the two-field NMR experiment for the measurement of proton longitudinal relaxation. Intensities are shown as black crosses together with their experimental uncertainty, the red curves represent the fitted mono-exponential decay.

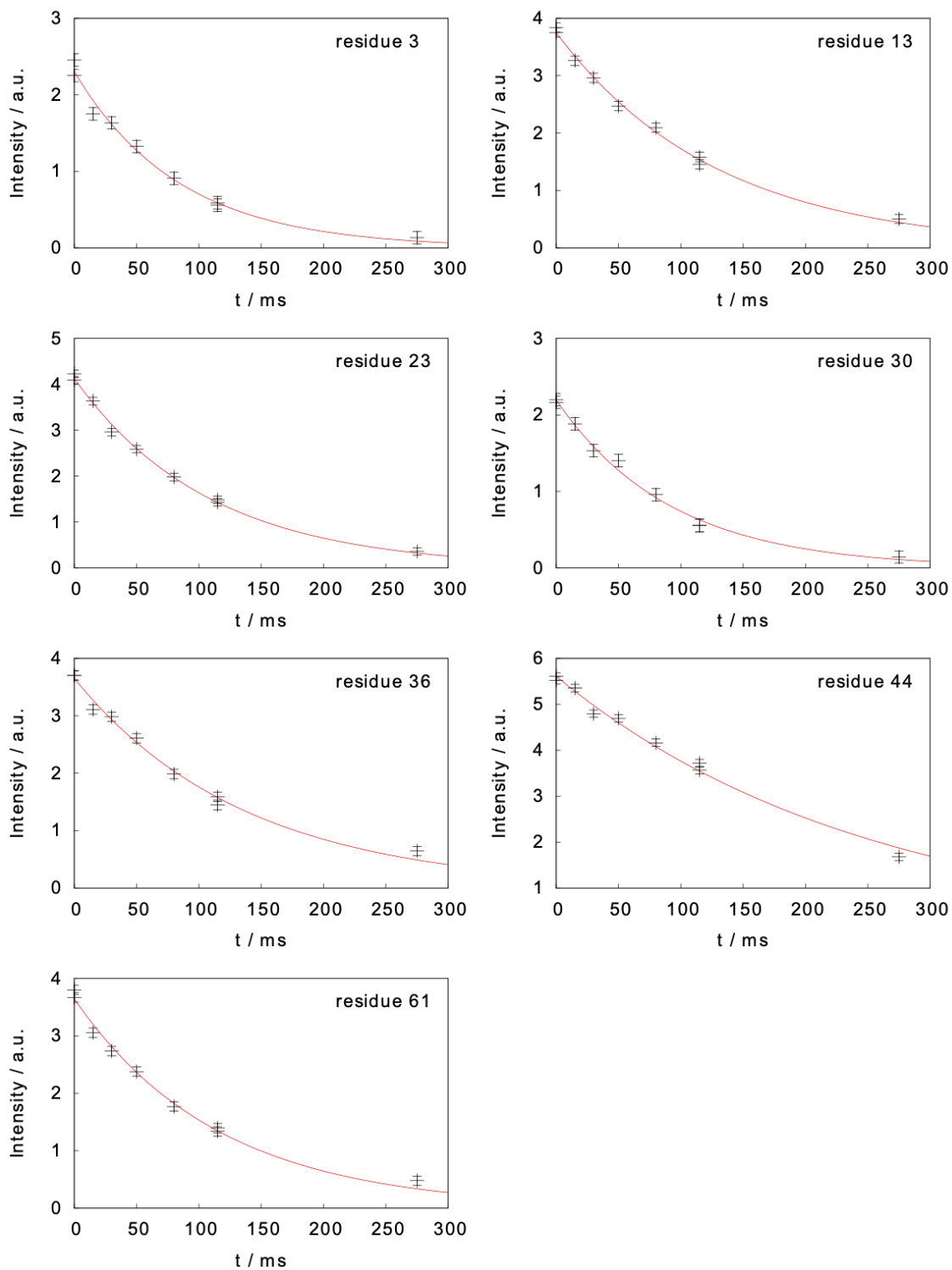


Figure S6. Measured intensity decays in the two-field NMR experiment for the measurement of proton $R_{1\rho}$ relaxation rates. Intensities are shown as black crosses together with their experimental uncertainty, the red curves represent the fitted mono-exponential decay.

Correlation function for the analysis of relaxation.

The motions of the CH bond are decomposed into three statistically independent motions. The correlation function $C_{CH}(t)$ is written as the product of three correlation functions:

$$C_i(t) = C_{met,i}(t)C_{axis}(t)C_g(t) \quad (S1)$$

$C_{met,i}(t)$ is the correlation function for the fast rotation of the methyl group about its symmetry axis, the subscript i defines the orientation of the principal axis of the interaction under consideration, here $i \in \{CH, CC, CD, HD\}$; $C_{axis}(t)$ describes the motions of the “symmetry” axis of the methyl group aligned with the CC bond; and $C_g(t)$ is the correlation function for overall rotational diffusion of the entire protein or domain. Fast rotation of the methyl group about its symmetry axis is described using the simple model-free correlation function $C_{met,i}(t)$:

$$C_{met,i}(t) = S_{met,i}^2 + (1 - S_{met,i}^2)\exp(-t/\tau_{met}) \quad (S2)$$

This rotation is axially symmetric, not isotropic, and the order parameter depends on the angle θ between the principal axis of the interaction and the methyl axis. At equilibrium, all orientations of the methyl group are equally probable, which leads to an order parameter $S_{met,i}^2 = [(3 \cos^2 \theta_i - 1)/2]^2$. For the CH dipole-dipole coupling, with an ideal tetrahedral geometry, $\theta_{ch} = 109.47^\circ$, and hence $S_{met,CH}^2 = 1/9$. We consider that the carbon-13 chemical shift anisotropy tensor is axially symmetric, with a principal axis aligned with the CC bond, and $S_{met,CC}^2 = 1$. Motions of the CC axis are described by the “extended model free” approach,^{44,46} with a correlation function $C_{axis}(t)$:

$$C_{axis}(t) = S_f^2 S_s^2 + (1 - S_f^2)\exp(-t/\tau_f) + S_f^2 (1 - S_s^2)\exp(-t/\tau_s) \quad (S3)$$

Motions in two different ranges of correlation times are accounted for in $C_{axis}(t)$: faster (resp. slower) motions are described by the order parameter S_f^2 (resp. S_s^2) and the correlation time τ_f (resp. τ_s). The overall rotational diffusion of the protein is described by an isotropic diffusion tensor defined by a single correlation time τ_c with a correlation function $C_{ov}(t) = (1/5)\exp(-t/\tau_c)$.

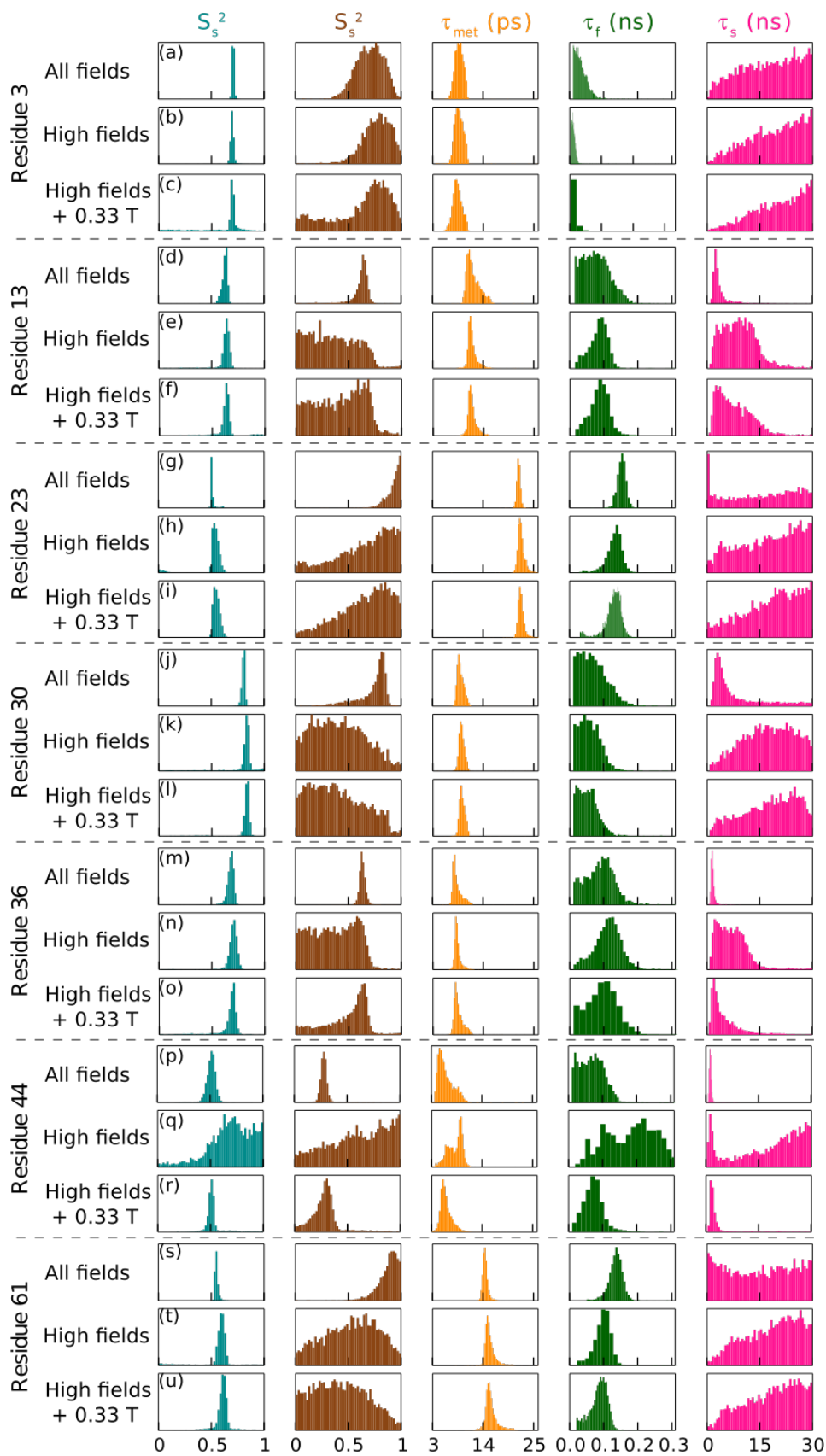


Figure S7. Parameters for internal dynamics obtained by the analysis of three sets of relaxation rates. S_f^2 and S_s^2 are order parameters associated with fast and slow motions of the $C^{\gamma_1}-C^{\delta_1}$ bond, respectively. Corresponding correlation times are τ_f and τ_s . τ_{met} is the correlation time for rotation of the methyl group. Results of analysis of all methyl group motions published earlier [1] are

presented. Analysis of relaxation at 20 magnetic fields [1] all longitudinal relaxation rates measured at fields $B_0 < 9$ T where measured with no rf pulse at low field are shown in rows (a), (d), (g), (j), (m), (p), and (s) (for detailed description of the dynamics parameters see [1]). Parameters obtained from the analysis of longitudinal, transverse relaxation and dipolar cross-relaxation rates at high field only (9.4 T; 14.1 T; 18.8 T; and 22.3 T) are shown in rows (b), (e), (h), (k), (n), (q), and (t). Analysis of the set of high field relaxation rates complemented by accurate longitudinal and transverse relaxation rates at 0.33 T measured with the two-field spectrometer are shown in rows (c), (f), (i), (l), (o), (r), and (u).

Table S3. Carbon longitudinal and transverse relaxation rates, and carbon-hydrogen dipole-dipole cross-relaxation rate at 22.3 T (950 MHz proton Larmor frequency) used in the MCMC analysis presented in Fig. S7. The residue number, longitudinal relaxation rate, transverse relaxation rate and carbon-proton cross-relaxation rates are shown in the first, second, and third respectively and were published earlier [1]. Chemical exchange affects relaxation rates of Ile-44 and its transverse relaxation rates were not included in the analysis.

Residue	$R_1 (^{13}\text{C}) / \text{s}^{-1}$	$R_2 (^{13}\text{C}) / \text{s}^{-1}$	$\sigma^{\text{NOE}} (^{13}\text{C}-^1\text{H}) / \text{s}^{-1}$
3	0.25 ± 0.003	2.18 ± 0.02	0.079 ± 0.001
13	0.36 ± 0.004	1.76 ± 0.02	0.113 ± 0.001
23	0.54 ± 0.005	1.90 ± 0.02	0.198 ± 0.002
30	0.29 ± 0.003	2.31 ± 0.02	0.085 ± 0.001
36	0.32 ± 0.003	1.84 ± 0.02	0.087 ± 0.001
44	0.31 ± 0.003	-	0.077 ± 0.001
61	0.42 ± 0.004	2.04 ± 0.02	0.144 ± 0.001

Table S4. Carbon longitudinal and transverse relaxation rates, and carbon-hydrogen dipole-dipole cross-relaxation rate at 18.8 T (800 MHz proton Larmor frequency) used in the MCMC analysis presented in Fig. S7. The residue number, longitudinal relaxation rate, transverse relaxation rate and carbon-proton cross-relaxation rates are shown in the first, second, and third respectively and were published earlier [1]. Chemical exchange affects relaxation rates of Ile-44 and its transverse relaxation rates were not included in the analysis.

Residue	$R_1 (^{13}\text{C}) / \text{s}^{-1}$	$R_2 (^{13}\text{C}) / \text{s}^{-1}$	$\sigma^{\text{NOE}} (^{13}\text{C}-^1\text{H}) / \text{s}^{-1}$
3	0.27 ± 0.004	2.10 ± 0.02	0.081 ± 0.002
13	0.39 ± 0.003	1.71 ± 0.02	0.119 ± 0.002
23	0.56 ± 0.005	1.88 ± 0.01	0.203 ± 0.003
30	0.32 ± 0.004	2.25 ± 0.02	0.088 ± 0.002
36	0.36 ± 0.003	1.73 ± 0.02	0.092 ± 0.002
44	0.34 ± 0.004	-	0.079 ± 0.002
61	0.44 ± 0.004	1.94 ± 0.02	0.151 ± 0.003

Table S5. Carbon longitudinal and transverse relaxation rates, and carbon-hydrogen dipole-dipole cross-relaxation rate at 14.1 T (600 MHz proton Larmor frequency) used in the MCMC analysis presented in Fig. S7. The residue number, longitudinal relaxation rate, transverse relaxation rate and carbon-proton cross-relaxation rates are shown in the first, second, and third respectively and were published earlier [1]. Chemical exchange affects relaxation rates of Ile-44 and its transverse relaxation rates were not included in the analysis.

Residue	$R_1 (^{13}\text{C}) / \text{s}^{-1}$	$R_2 (^{13}\text{C}) / \text{s}^{-1}$	$\sigma^{\text{NOE}} (^{13}\text{C}-^1\text{H}) / \text{s}^{-1}$
3	0.34 ± 0.006	2.04 ± 0.02	0.079 ± 0.002
13	0.46 ± 0.005	1.66 ± 0.01	0.121 ± 0.003
23	0.64 ± 0.006	1.84 ± 0.01	0.220 ± 0.004
30	0.40 ± 0.006	2.17 ± 0.02	0.086 ± 0.002
36	0.44 ± 0.005	1.67 ± 0.013	0.096 ± 0.002
44	0.41 ± 0.006	-	0.088 ± 0.002
61	0.51 ± 0.005	1.89 ± 0.01	0.156 ± 0.003

Table S6. Carbon longitudinal and transverse relaxation rates, and carbon-hydrogen dipole-dipole cross-relaxation rate at 9.4 T (400 MHz proton Larmor frequency) used in the MCMC analysis presented in Fig. S7. The residue number, longitudinal relaxation rate, transverse relaxation rate and carbon-proton cross-relaxation rates are shown in the first, second, and third respectively and were published earlier [1]. Chemical exchange affects relaxation rates of Ile-44 and its transverse relaxation rates were not included in the analysis.

Residue	$R_1 (^{13}\text{C}) / \text{s}^{-1}$	$R_2 (^{13}\text{C}) / \text{s}^{-1}$	$\sigma^{\text{NOE}} (^{13}\text{C}-^1\text{H}) / \text{s}^{-1}$
3	0.49 ± 0.04	2.22 ± 0.10	0.077 ± 0.009
13	0.62 ± 0.03	1.67 ± 0.08	0.125 ± 0.011
23	0.74 ± 0.03	1.90 ± 0.07	0.229 ± 0.017
30	0.57 ± 0.04	2.29 ± 0.10	0.091 ± 0.010
36	0.62 ± 0.03	1.75 ± 0.08	0.108 ± 0.010
44	0.52 ± 0.03	-	0.110 ± 0.010
61	0.62 ± 0.03	2.05 ± 0.07	0.162 ± 0.013

Table S7. Median values and standard deviations for fitted parameters shown in the distributions in Figure S7 “all fields”. Results were obtained after a Markov-Chain Monte-Carlo on corrected high-resolution relaxometry data and high-field data.

	S_f^2			S_s^2			CSA (ppm)		
	Median	+ σ	- σ	Median	+ σ	- σ	Median	+ σ	- σ
3	0.71	0.01	0.01	0.76	0.12	0.15	23.8	1.57	1.43
13	0.63	0.02	0.03	0.62	0.06	0.15	23.9	2.53	2.33
23	0.51	0.01	0.01	0.90	0.07	0.12	20.1	1.36	1.37
30	0.81	0.01	0.02	0.74	0.10	0.30	22.5	2.05	2.19
36	0.67	0.02	0.02	0.58	0.03	0.03	29.4	1.28	1.19
44	0.51	0.03	0.05	0.28	0.02	0.03	Not fitted		
61	0.55	0.02	0.01	0.89	0.07	0.11	26.1	1.87	1.83

	τ_{met} (ps)			τ_f (ps)			τ_s (ns)		
	Median	+ σ	- σ	Median	+ σ	- σ	Median	+ σ	- σ
3	8.56	1.06	0.88	34.8	24.4	17.0	17.7	8.86	10.6
13	11.5	1.85	0.94	77.3	40.7	39.3	3.13	4.10	1.08
23	21.7	0.38	0.33	150	11.8	12.1	18.3	8.37	11.4
30	9.03	0.92	0.61	61.8	47.6	35.4	6.98	14.8	4.20
36	8.05	1.14	0.43	82.8	24.8	37.6	2.48	0.63	0.45
44	5.58	2.44	1.17	70.3	42.1	42.9	1.27	0.36	0.22
61	14.4	0.71	0.45	138	18.2	26.1	17.3	9.05	12.7

Table S8. Median values and standard deviations for fitted parameters shown in the distributions in Figure S7. Results were obtained after a Markov-Chain Monte-Carlo high-field data only. CSA was kept constant to the median value shown in Table S7.

	S_f^2			S_s^2		
	Median	+ σ	- σ	Median	+ σ	- σ
3	0.70	0.01	0.01	0.78	0.12	0.14
13	0.64	0.03	0.03	0.34	0.27	0.24
23	0.54	0.03	0.03	0.71	0.20	0.33
30	0.83	0.02	0.04	0.40	0.28	0.25
36	0.71	0.03	0.03	0.37	0.23	0.25
44	0.70	0.20	0.20	0.63	0.28	0.35
61	0.60	0.03	0.04	0.54	0.25	0.29

	τ_{met} (ps)			τ_f (ps)			τ_s (ns)		
	Median	+ σ	- σ	Median	+ σ	- σ	Median	+ σ	- σ
3	8.76	1.00	0.89	30.8	19.8	14.2	20.8	6.61	9.56
13	11.4	1.07	0.52	91.2	27.4	33.6	8.98	4.70	4.97
23	22.2	0.82	0.49	136	18.5	23.0	19.2	7.62	10.6
30	9.26	0.66	0.48	65.3	2x10 ³	36.1	18.1	7.53	8.42
36	8.21	0.66	0.38	114	34.8	41.4	6.50	4.28	3.76
44	8.56	1.04	2.37	3x10 ³	16x10 ³	3x10 ³	21.2	6.38	15.8
61	15.2	1.08	0.57	103	30.2	25.6	19.9	6.69	9.66

Table S9. Median values and standard deviations for fitted parameters shown in the distributions in Figure S7. Results were obtained after a Markov-Chain Monte-Carlo on accurate carbon longitudinal and transverse relaxation rates at 0.33 T measured in this study and high-field data.

	S_f^2			S_s^2		
	Median	+ σ	- σ	Median	+ σ	- σ
3	0.69	0.02	0.23	0.71	0.16	0.42
13	0.64	0.02	0.03	0.43	0.22	0.29
23	0.54	0.03	0.03	0.70	0.20	0.29
30	0.83	0.02	0.02	0.36	0.32	0.24
36	0.69	0.03	0.06	0.55	0.10	0.30
44	0.51	0.02	0.03	0.28	0.07	0.11
61	0.61	0.03	0.04	0.40	0.28	0.26

	τ_{met} (ps)			τ_f (ps)			τ_s (ns)		
	Median	+ σ	- σ	Median	+ σ	- σ	Median	+ σ	- σ
3	8.31	1.08	0.90	45.0	9×10^3	23.9	21.5	6.33	8.81
13	11.3	0.92	0.52	91.6	28.7	31.6	6.74	5.96	3.76
23	22.2	0.71	0.48	132	16.6	22.6	19.9	7.16	10.1
30	9.34	0.72	0.49	53.3	35.6	29.4	19.0	7.03	10.0
36	8.29	1.29	0.56	105	82.8	53.9	3.38	5.43	1.68
44	5.85	1.43	0.74	74.1	35.1	28.3	1.83	1.43	0.50
61	15.4	1.26	0.68	94.4	33.6	30.0	20.0	6.73	9.33

Reference:

[1] Cousin, S.F.; Kadeřávek, P.; Bolik-Coulon, N.; Gu, Y.; Charlier, C.; Carlier, L.; Brüschweiler-Li, L.; Marquardsen, T.; Tyburn, J.M.; Brüschweiler, R.; Ferrage, F., Time-resolved protein side-chain motions unraveled by high-resolution relaxometry and molecular dynamics simulations *J. Am. Chem. Soc.* **2018**, 140, 13456-13465.